

# Assessment of elemental distributions at line and planar defects in Cu(In,Ga)Se<sub>2</sub> thin films by atom probe tomography

Oana Cojocar-Mirédin<sup>1,2,\*</sup> Torsten Schwarz<sup>2</sup> and Daniel Abou-Ras<sup>3,\*</sup>

<sup>1</sup>RWTH Aachen, I. Physikalisches Institut IA; Sommerfeldstraße 14, 52074 Aachen, Germany.

<sup>2</sup>Max-Planck-Institut für Eisenforschung GmbH, Max-Planck-Straße 1, 40237 Düsseldorf, Germany

<sup>3</sup>Helmholtz-Zentrum Berlin für Materialien und Energie GmbH, Hahn-Meitner-Platz 1, 14109 Berlin, Germany.

[cojocar-miredin@physik.rwth-aachen.de](mailto:cojocar-miredin@physik.rwth-aachen.de)

[daniel.abou-ras@helmholtz-berlin.de](mailto:daniel.abou-ras@helmholtz-berlin.de)

Keywords: Cu(In,Ga)Se<sub>2</sub>, grain boundaries, twin boundaries, impurity segregation, correlative microscopy,

## Abstract

Thin-film solar cells with polycrystalline Cu(In,Ga)Se<sub>2</sub> absorber layers exhibit record power-conversion efficiencies of currently 22.6%. Such performance is impressive in view of the rather small average grain sizes of 0.5-1.5 μm with Cu(In,Ga)Se<sub>2</sub> layer thicknesses of 2-3 μm. The present work gives insight to the chemistry at linear and planar defects in Cu(In,Ga)Se<sub>2</sub> thin films, describing in detail how to access the corresponding information on the nanometer scale by means atom-probe tomography. Moreover, we showed here how the tip sample can be investigated by transmission electron microscopy prior to the atom-probe tomography experiments to determine the structure of the planar defects. Based on various results presented here, it can be stated that a common feature of planar defects in Cu(In,Ga)Se<sub>2</sub> thin films is an atomic redistribution occurring at the lattice planes adjacent to the planar defects. The results from atom-probe tomography are compared with those from theoretical predictions, and consequences for the energy-band diagrams around these planar defects are proposed. When correlating the gathered compositional information at planar defects with results from microscopic electrical analyses at the planar defects as well as with those from two-dimensional device modeling, enhanced non-radiative (Shockley-Read-Hall) recombination, mainly at random grain boundaries, is highlighted as one possible origin for the limited open-circuit voltage of the Cu(In,Ga)Se<sub>2</sub> solar cells.

## 1. Introduction

Nowadays, enhanced understanding of the relationships for extended structural defects in semiconductor compounds is needed, as, e.g., those used in solar cells. Indeed, in these devices, various line and planar defects, i.e., (partial) dislocations, stacking faults (SFs), twin boundaries (TBs) as special cases of SFs, and random grain boundaries (GBs), can be considered in general electrically active, exerting substantial influence on the electrical properties of the entire device [1].

Out of the various solar cell technologies currently under investigation, those using Cu(In,Ga)Se<sub>2</sub> (CIGS) absorber layers exhibit the highest conversion efficiencies of up to 22.6% [2]. Regarding the polycrystalline nature of the CIGS thin films, enhanced understanding of how the microstructure influences the device performance is of particular importance for the further improvement of the CIGS technology. Part of the related investigations concerns the analysis of structure and composition at and around line and planar defects in CIGS thin films, which needs to be performed at the nanometer and subnanometer scale.

For these investigations, it is crucial to link the detected chemical changes to the structures of line and planar defects, in order to correlate the compositional information with the type of the extended structural defect. Therefore, correlative studies at identical specimen positions are required. One possibility is to apply high-resolution imaging in (scanning) transmission electron microscopy ((S)TEM) and its related techniques electron energy-loss spectroscopy (EELS) as well as energy-dispersive X-ray spectroscopy (EDX), which are able to characterize both, chemical and structural properties of extended defects [3]. However, since EELS and EDX can detect impurities only down to concentrations of about 0.1 at.%, the corresponding compositional information is limited.

As an alternative, the current work will give details on a combinatory approach, comprising first diffraction-contrast imaging and electron diffraction in TEM, and secondly atom-probe tomography (APT), comprising field-evaporation of a tip-shaped specimen and detection of the evaporated sample atoms employing mass spectroscopy, in order to eventually obtain the three-dimensional reconstruction of the APT tip. For the investigation of the structures of extended defects, diffraction techniques in TEM are excellent tools, e.g., when interested in crystallographic grain orientations [4] or in the misorientation angle for a specific GB [5]. In some cases, it is even possible to determine the boundary plane when utilizing the trace of the interface [6]. Particularly, scanning nanobeam diffraction and Kikuchi diffraction have been used frequently for crystallographic orientation determination in polycrystalline materials with grain sizes of between 10 nm and up to several 100  $\mu\text{m}$ , in combination with APT analyses. Herbig et al. [7] showed the feasibility of using the scanning nanobeam diffraction technique for determining the grain orientation directly on an APT tip fabricated from a nanocrystalline pearlite material prior to the actual APT experiment. Babinski et al. [8] used the transmission Kikuchi diffraction technique (TKD) in scanning electron microscopy (SEM) to obtain the grain orientations directly on the APT tip prepared from a polycrystalline Mo sample, which contained P, N, and O impurities.

In the present work, we provide details on how to apply the approach of correlative APT-TEM studies on brittle material systems, using the example of polycrystalline CIGS absorber layers as a model system. We will provide an overview of compositional data obtained by APT at various line and planar defects in different CIGS thin films, as well as with a comparison with the corresponding results obtained by (S)TEM-EELS. Finally, the structure and composition of the extended defects will be linked to the device performance of the CIGS solar cells, providing a possible reason for the limitation of the open-circuit voltage in these devices.

## **2. Experimental procedure**

### **2.1 Solar cell production and performance**

Various CIGS absorbers had been studied in this paper as described in **Table 1** by sample A, B, and C. All the CIGS absorbers were prepared using a three-stage coevaporation process or interrupted three-stage coevaporation process either at Helmholtz Zentrum Berlin (HZB) [9,

10] or at Zentrum für Sonnenenergie- und Wasserstoffforschung (ZSW) Stuttgart [11]. The solar cells consisted of a ZnO/CdS/CIGSe/Mo stack on a soda-lime glass substrate (containing mainly Na<sub>2</sub>O, K<sub>2</sub>O, and SiO<sub>2</sub>) with relatively high power-conversion efficiency, i.e., of more than 15 %. During the growth of the coevaporated CIGS layer on top of the sputtered Mo thin film, Na, K, and also O tend to diffuse from the substrate into the growing CIGS layer (see, e.g., Ref. [12]).

For the study of SFs (see sample B in **Table 1**) described in the present work, the CIGS absorber was prepared using a SiN diffusion barrier between Mo and the CIGS substrate to prevent uncontrolled Na diffusion from the glass in the film. Moreover, for this specific sample the CIGS second step in the three-stage process (Cu-Se deposition at 430 °C) was interrupted before the film composition became Cu-rich ( $[Cu]/([In]+[Ga]) > 1$ ) [9]. The 3-stage coevaporation process was interrupted in order to understand why the Cu-poor CIGS absorber obtained without experiencing a Cu-rich step has a poorer quality than the standard CIGS absorber. It turns out that this is mainly due to the high density of planar defects present in the absorber, defects which enhances the recombination activity inside the cell.

Sample	Studied defects	Fabrication procedure	Barrier layer at Mo/CIGS	$\frac{[Cu]}{[In] + [Ga]}$ $\frac{[Ga]}{[In] + [Ga]}$	Efficiency	Manufacturing place
<b>A</b>	linear defects (dislocations)	3-stage coevaporation process [10]	no	$\sim 0.96/\sim 0.28$ /	$\sim 19\%$	HZB, Germany
<b>B</b>	planar defects (SFs)	interrupted 3-stage coevaporation process [9]	yes (SiN diffusion barrier layer)	$\sim 0.71/\sim 0.24$	-	HZB, Germany
<b>C</b>	planar defects (GBs)	3-stage coevaporation process [11]	no	$\sim 0.75/\sim 0.3$	$\sim 15\%$	ZSW, Germany

**Table 1.** General overview of the CIGS solar cells used in the present study.

## 2.2 Analysis conditions of APT

Atom probe tips were prepared utilizing a dual-focused ion beam (FIB) (FEI Helios Nanolab 600i) using a lift-out procedure described in Ref. [13]. Commercial Mo TEM grids were cut into two halves and electropolished in order to use them as posts for placing chunks from the lift-out. These half-grids were then mounted in an in-house designed single-tilt TEM retainer, which together with appropriate adapters can also be used for FIB milling and APT measurements [14]. The APT tips were sharpened using a Ga<sup>+</sup> ion beam with an acceleration voltage of 16 kV. Final tip cleaning was performed under low-voltages conditions of 2-5 kV to minimize Ga beam damage. TEM studies on the APT tips were carried out in a JEOL JEM-2200FS microscope operated at an acceleration voltage of 200 kV.

APT experiments were performed with a local electrode atom probe (LEAP 3000X HR, Cameca Instruments), applying laser pulses of 532 nm wavelength, 12 ps pulse length, and an energy of 0.1 nJ per pulse at a repetition rate of 100 kHz. The specimen base temperature was

about 60K. Under these conditions, most of the detected events are single events (~80 %). However, the mass spectrum from **Figure 1** show the presence of numerous molecular ions such as  $\text{CuSe}^+$ ,  $\text{Cu}_2\text{Se}^+$ ,  $\text{CuSe}_2^+$ ,  $\text{Se}_2^+$ ,  $\text{Se}_2^{2+}$ ,  $\text{Se}_3^+$ . No molecular ions were detected for In or Na, O, and K impurities. Moreover, the correlation histogram for the evaporation of the CIGS layer (not shown here) shows no signature for molecular ion dissociation that may occurs after field evaporation either in LEAP 3000X HR nor in LEAP 4000X Si as it had been observed by David Saxey [15] for the GaN compound. Thus, the molecular ions from **Figure 1** are the ‘parents ions’. The absence of both, In-related molecular ions and dissociation of Cu-related molecular ions, can be explained by the weaker In-Se bonds compared to the stronger Cu-Se bonds as proved by Merino et al. [16] (the bonding length of In-Se is 0.258 nm, whereas for Cu-Se, it is 0.241 nm in the  $\text{CuInSe}_2$  chalcopyrite-type crystal structure).

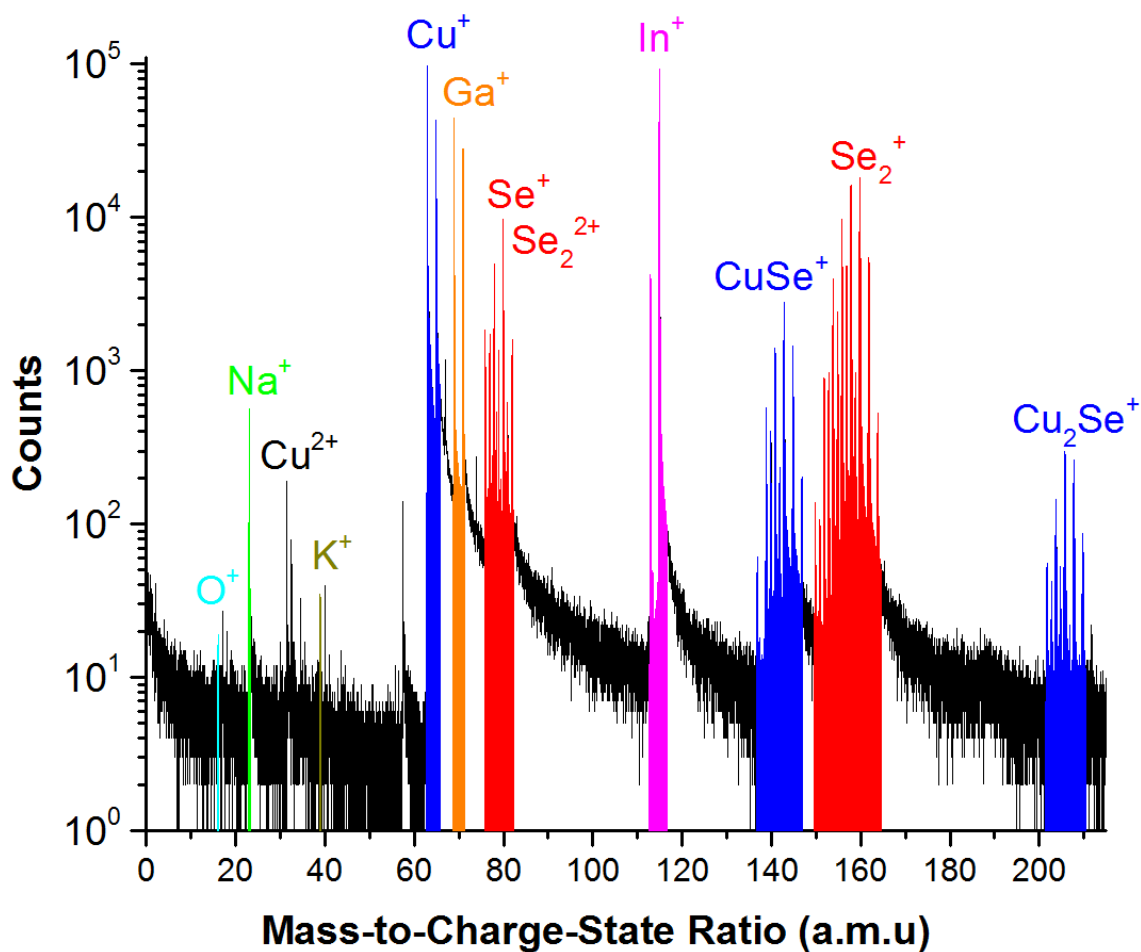


**Figure 1.** Mass spectrum showing the counts versus the mass-to-charge-state ratio of a CIGS absorber containing one GB.

### 2.3. Limitations of APT studies on CIGS thin films

The first limitation of the APT studies when dealing with CIGS material is the peak overlap of elements having the same mass-to-charge ratio in the mass spectrum. For example, the isotopes  $^{39}\text{K}^+$  and  $^{41}\text{K}^+$  overlap with  $^{78}\text{Se}^{2+}$  and  $^{82}\text{Se}^{2+}$  at 39 a.m.u. and 41 a.m.u., respectively. The excess of K at GBs can be still determined if the Se concentration does not change, as shown by

Schwarz et al. [17]. To overcome this issue, single atom detectors with kinetic energy discrimination are required [18]. Such a detector could likely also reduce noise and, hence, increase the sensitivity with respect to impurities. Moreover, false imaging, i.e. wrong assignment of atoms to an element, in atom probe maps would be significantly reduced by discrete discrimination [18]. Other peak overlaps detected in the mass spectrum of the CIGS compound from **Figure 1** are  $^{16}\text{O}^+$  and  $^{32}\text{O}_2^{2+}$  and  $^{76,77,78,80,82}\text{Se}^+$  and  $^{152,154,156,160,164}\text{Se}_2^{2+}$ . Here, only peak decomposition of overlapping peaks by using the natural isotopic abundancies, which is referred to collective discrimination, can help to determine the correct composition.

The second main limitation of APT is the detection efficiency of the single atom detector. The detection efficiency, which is equal for each element, is limited to ~40-60% in commercially used APT instruments due to geometrical constraints of the microchannel plate (MCP) used as detector [19]. Since 2015, APT facilities with 80% detection efficiency [19, 20] are available at Cameca Instruments Inc. This increase will improve, for instance, the analysis of nanoclusters and solutes, e.g. that of Na and K. However, a new detector design is needed to achieve 100% detection efficiency.

The third limitation of the APT technique is the impossibility to determine with an accuracy better than 1-2 nm the widths of GBs or other extended defects. This spatial limitation is due to the so-called ‘local-magnification effect’, which leads to aberrations of ion trajectories due to a difference in the electric field strengths required for field-evaporation of atoms in the grain interior and at e.g. the GB [21]. This effect leads to lateral displacements of atoms and subsequently to density fluctuations and, hence, to a broadening of GB width. This effect is most striking at GB planes being parallel to the analysis direction [21]. Therefore, comparison of absolute impurity concentration at various GBs based only on the 1D concentration profile is not accurate [22]. In order to correctly quantify the amount of impurities segregated at GBs or other defects, one needs to use the so called ‘Gibbsian interfacial excess’, which represents the number of excess impurity atoms at an interface normalized to its area [23].

### 3. Results

#### 3.1 TEM-APT correlative approach

A possible approach to reveal both, structural and chemical features at lattice defects is based on correlative (S)TEM-APT. A very important issue when dealing with correlative TEM-APT is the quality of the APT tips prepared by FIB milling. Ion-beam-induced amorphisation and Ga, C contamination [24] are indeed very often observed. The ion-beam-induced amorphisation at various acceleration voltages had been studied for CIGS material as depicted in **Figure 2**. We observed that a 30 kV acceleration voltage will create a 30 nm amorphous layer at the apex of the tip and approximatively 13 nm on the sidewalls of the tip. It is thus expected that this amorphous layer will drastically decrease the quality of diffraction pattern (DP) and transmission Kikuchi pattern (TKP) quality.

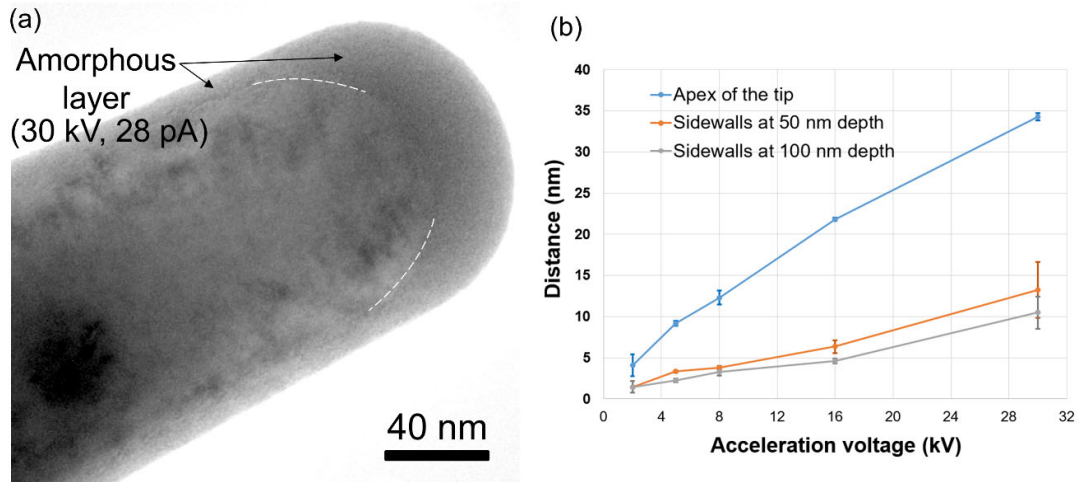


**Figure 2.** (a) TEM image showing the  $\text{Ga}^+$ -beam induced amorphisation at the apex and sidewalls of the APT tip at 30 kV acceleration voltage. (b) The  $\text{Ga}^+$ -beam induced amorphisation distance at the apex and sidewalls of the atom probe tip versus the acceleration voltage. These distances were measured from the TEM images.

Extensive transmission electron forward scattered diffraction (t-EFSD or t-EBSD) had been done recently to determine the structure of GBs [8]. Moreover, we showed recently that the sharpness of TKP depends generally on the procedure used to prepare them (excluding TKP blurring when the crystal is highly deformed containing a high dislocation density) [25]. **Figure 3** shows the TKP collected in TEM at 30 kV, 16 kV, 8 kV, 5 kV, and 2 kV acceleration voltage used for FIB milling. The Kikuchi bands and lines are clearly visible in all TKPs independently of the applied acceleration voltage, but with sharper Kikuchi lines when the APT tip was prepared in low-kV mode. This is mainly due to the 200 kV electron beam energy used for TEM, which is ten times higher than the acceleration voltage used for t-EFSD. Indeed, at lower electron beam energies the excited volume is located very close to the surface of the APT tip which had been exposed to the  $\text{Ga}^+$  beam, whereas at higher electron beam energies the excited volume is located deeper inside the volume of the tip and thus less sensitive to the tip's surface quality. Moreover, the use of 200 kV acceleration voltage in TEM explains also why obtaining TKP from a relatively thick APT tip (between 200 nm and 300 nm) is possible in TEM, but not in t-EBSD.

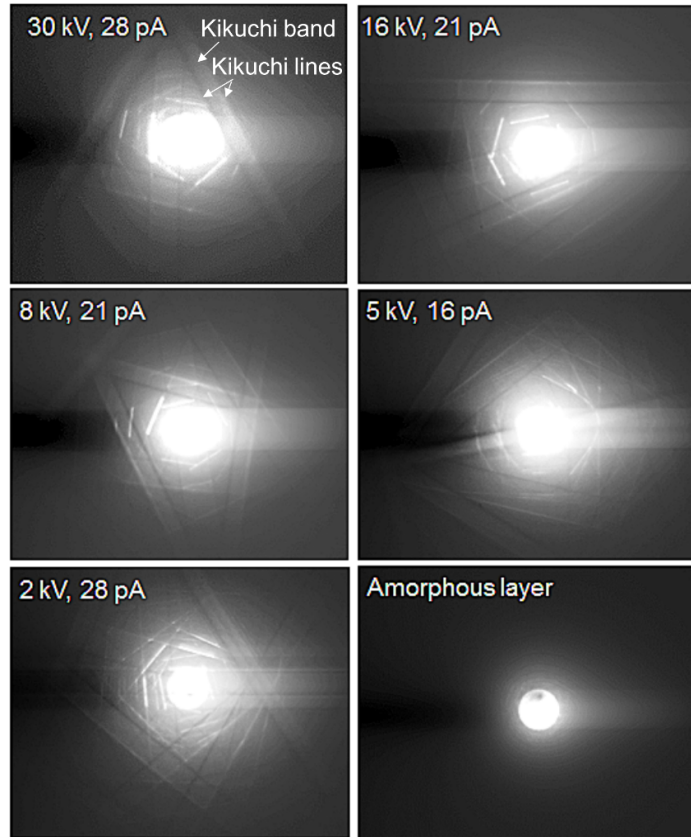


**Figure 3.** Transmission Kikuchi patterns (TKP) collected at 30 kV, 16 kV, 8 kV, 5 kV, and 2 kV acceleration voltage using low currents (between 15 pA and 30 pA) for the Ga<sup>+</sup>-beam. These patterns were collected using the STEM in spot-mode (1.5 nm spot size).

Thus, the main advantage of using the STEM for TKP acquisition is that the Kikuchi bands are clearly visible on the TKP even when the atom probe tips were prepared using a high-acceleration voltage in the FIB. Nevertheless, we still performed a fast low-kV cleaning in order to remove any Ga-contamination from the tips. Moreover, with TEM and high-resolution TEM we can readily determine the GB curvature by orienting one of the grains in Bragg conditions. This approach enables the user to understand the *coherency* (when the local plane normal corresponds with the mirror plane of the boundary) and *asymmetry* (different hkl in the adjacent grains) at the GB. This information is not readily available after performing a standard t-EFSD 2D mapping because of the limited resolution of about 10-20 nm [26]. It is well known that pattern overlap at GBs may cause some uncertainty in the t-EFSD measurements. A realistic information about the GB curvature will be obtained only when the t-EBSD investigations are performed for different rotation angles of the tip (at least for 0°, 45°, and 90°). Of course, this will induce supplementary C-contamination on the tip.

In the following two subsections we will show how we investigated the structure of SFs and GBs with TEM, prior to the APT investigations.

### 3.1.1 Stacking faults

**Figure 4** shows one of APT tip obtained from sample B and further investigated by STEM. A high density of strip structures was detected in the absorber layer, as shown also on the zoomed area in **Figure 4** (b) and (d). These strip structures are most likely SFs or/and microtwins. To elucidate which planar defects were observed by STEM, several diffraction patterns were acquired from this specific area. **Figure 4** (c) shows one of these diffraction patterns. Such

elongated spots in the diffraction patterns, i.e. such streak patterns are typical signatures for the SFs [27]. The (112) lattice planes are found to have dense SFs, as it is highlighted in **Figure 4** (c).

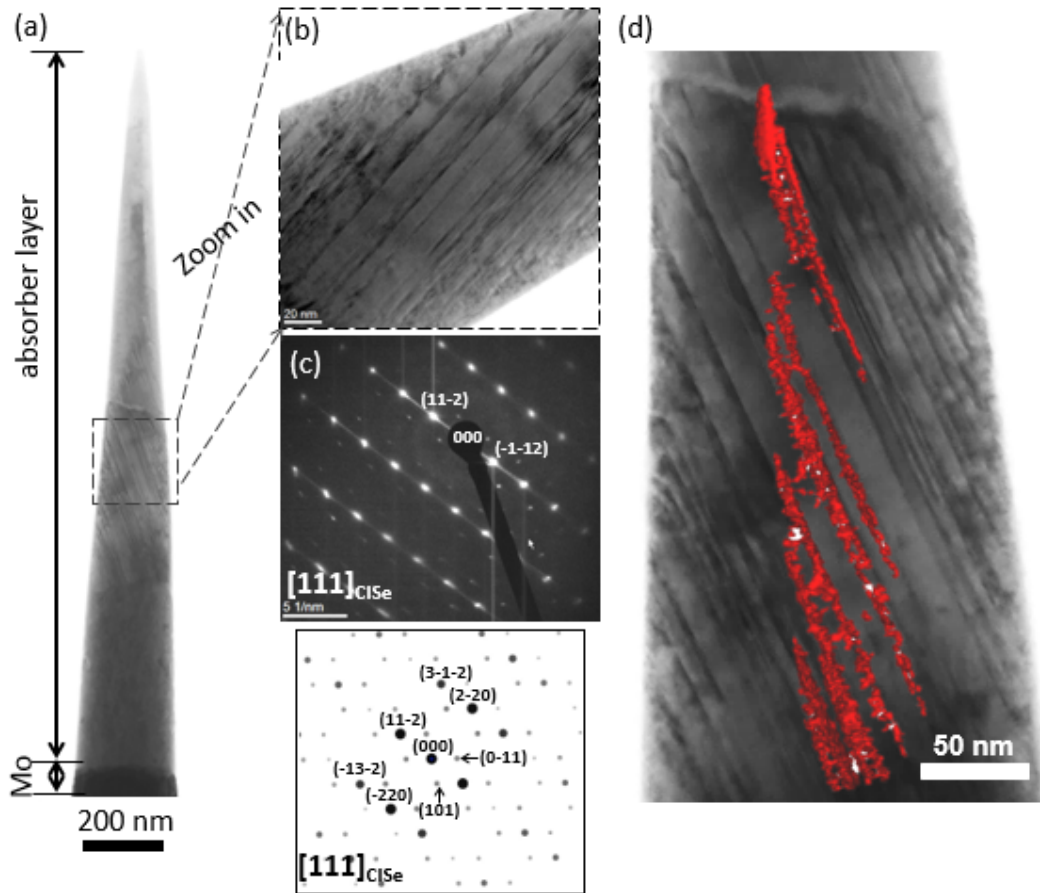


**Figure 4.** (a) Bright-field STEM micrograph of the CIGSe and Mo layers of the sample B. (b) TEM image of the region containing numerous Stacking faults in CIGS absorber, (c) the diffraction pattern from the region highlighted in (b), and (d) the overlap between the STEM image and Se iso-density surfaces map (obtained from the APT data).

### 3.1.2 Twin boundary and random high-angle grain boundary

**Figure 5** and **Figure 6** show two typical examples of (S)TEM investigations conducted on twin boundaries (TBs) and random high-angle GBs (HAGBs) obtained from the CIGS absorber of sample C. The tips containing either a TB or a GB are investigated in (S)TEM and tilted along the x-axis of about  $+14.3^\circ$  and  $+12.4^\circ$ , respectively, so that the upper grain region is in Bragg condition and thus the boundary plane is clearly revealed. The orientation determination of grain regions  $G_1$  and  $G_2$  was performed using the STEM probe in spot mode and thus obtaining the diffraction information from a small region ( $<10$  nm). In this way the TKP was collected for each grain, directly adjacent to the GB. The main advantage of using the TKP is the high accuracy of the orientation determination which can be better than  $0.1^\circ$  at a spatial orientation resolution estimated to be around 10 nm [28]. The TKPs shown in **Figure 5** and **Figure 6** were acquired under the following conditions: 0.7 nm spot size, 25 cm camera length and condenser lens aperture of 20  $\mu\text{m}$  diameter. The indexing of the TKP, i.e. the calculation of the crystal orientation from the indexed vectors, was done using the commercial software TOCA [29].

This manual measurement routine is well suited for the present case since only few grains are detected on each atom probe tip.

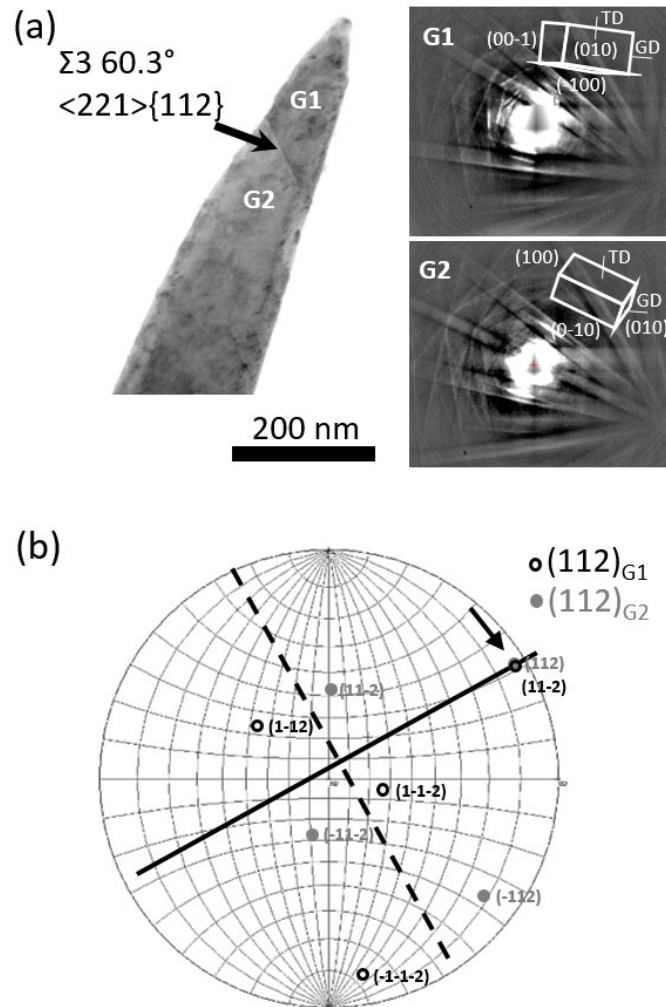


**Figure 5** (a). Bright-field TEM picture of the APT tip showing a  $\Sigma 3$  TB plane and the two neighboring grains, referred here to as  $G_1$  and  $G_2$  in CIGS absorber from sample C. Kikuchi patterns taken from both grains  $G_1$  and  $G_2$  are shown. By indexing the TKPs of regions  $G_1$  and  $G_2$  the calculated misorientation angle was  $60.3^\circ$  with a deviation angle of  $0.1^\circ$ . (b) Stereographic projection displaying all possible symmetrically equivalent planes from  $G_1$  and  $G_2$ , the boundary trace (dashed line) and the boundary plane normal (thick continuous line).

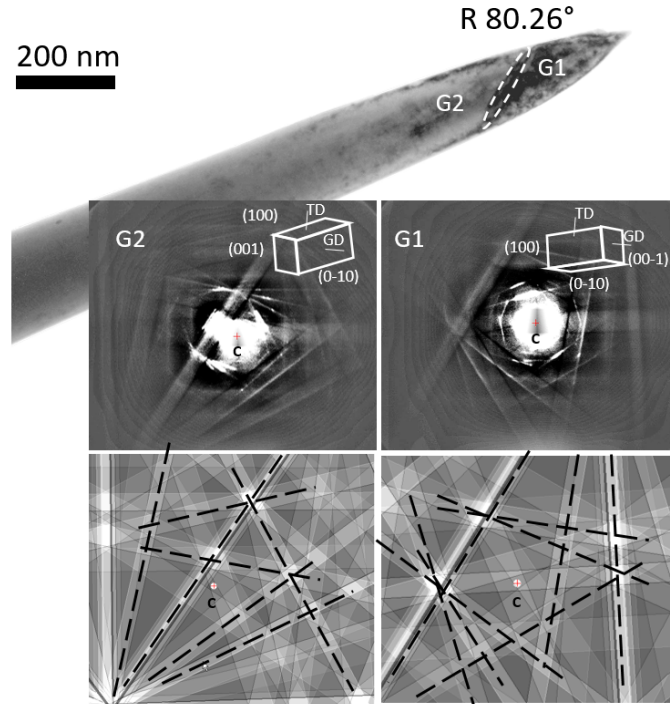


**Figure 6.** Bright-field TEM picture of the atom probe tip showing the GB plane and the two neighboring grains G1 and G2 in CIGS absorber from sample C. Below TKPs taken from G1 and G2 and the respective recalculated patterns are shown. By indexing the TKP of G1 and G2 the calculated misorientation angle was  $80.26^\circ$  with a deviation angle of  $0.1^\circ$ .

By using this method several TBs and GBs were investigated. **Figure 5** and **Figure 6** show a coherent  $\Sigma 3$  TB and a random HAGB and with  $60.3 \pm 0.1^\circ$  and  $80.26 \pm 0.1^\circ$  misorientation angles, respectively. **Figure 5** (b) illustrates the stereographic projection of all possible symmetrically equivalent planes acquired from the two grains adjacent to the GB. Taking into account the GB plane orientation, *i.e.* the trace of the boundary observed in the STEM image (not shown here), one can readily determine the GB plane normal as proved in the recent work of Stoffers et al. [30]. We note here that the dotted line inserted in **Figure 5** (b) marks the GB trace which is perpendicular to the GB plane normal shown by a thick continuous line. Thus, it is clearly demonstrated that the  $\Sigma 3$  TB lies exactly on a (112) plane.

## 3.2 Detailed APT investigations on extended defects

### 3.2.1 Elemental distribution at line defects

In **Figure 7** (a), a reconstructed three-dimensional APT data cube is depicted, which gives the Na and Se distribution within a section of a polycrystalline CIGS thin film of the sample A. The Na signal is enhanced within two lines, which can be related to dislocation cores. **Figure 7** (b) shows line scans extracted from the APT data around one of the linear features (D1 in **Figure 7** (a)). Local maxima are visible in the Na and K signals, while the Cu signal is reduced considerably.

Moreover, the Na and Cu signals exhibit different full widths at half maximum/minimum of 1.5 and 3 nm. In contrast, the In, Ga, and Se signals do not change substantially within the errors of measurement, and the O signal remains below the noise level throughout the measured specimen volume. We note that the elemental distributions around the linear feature D2 shown in **Figure 7** (a) are similar. It should be mentioned that up to date, only very few APT data cubes actually exhibit linear features with compositional changes. Therefore, the statistics on

elemental distributions across dislocations is very poor. Nonetheless, these linear features can be distinguished well from stacking faults and grain boundaries, which are planar defects and hence exhibit changes in composition along a plane in the APT 3D data.

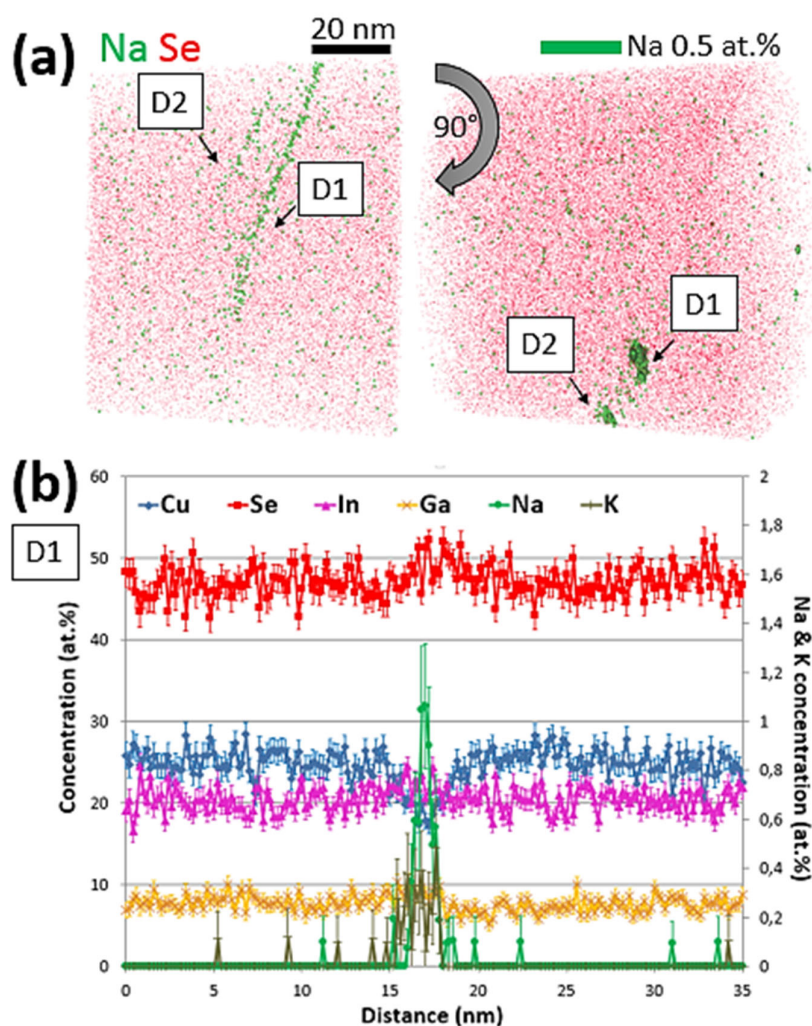


**Figure 7.** Reconstructed, three-dimensional APT data cube of a CIGS crystal from sample *A* exhibiting the Na (green) and Se (red) distribution across the crystal. The Na signal is enhanced within two linear features, which can be related to dislocation cores.

### 3.2.2 Elemental distribution at high-symmetrical planar defects

**Figure 8** (a) shows the 3D reconstruction of a fraction of the Cu, In, Ga, and Se atoms at the SFs preinvestigated by the (S)TEM as shown in **Figure 4**. These SFs were present in a CIGS absorber layer where no Na impurity was present, since a SiN diffusion barrier was deposited on the glass substrate. A higher atomic density was observed at these SFs, as revealed by the Se-density profile in **Figure 8** (b). The higher atomic density at these planar defects can be due to local magnification effect [21], since no change in mass density is expected for intrinsic (ABCAB/ABC stacking sequence) or extrinsic (ABCAB/A/CABC stacking sequence) SFs. Combining Se iso-density surfaces (density of the ions, by ion count) with the STEM map in **Figure 4** (d) clearly reveals the good agreement between the APT and TEM measurements and enables for the first time a joint structural and chemical characterization at exactly the same position of such features.

**Figure 8** (b) shows the linear concentration profiles for Cu, In, Ga, and Se through four consecutive SFs. All the SFs detected in this volume reveal the same trend: Cu-depletion and

In-enrichment ('In on Cu'). Some of the SFs show also Se enrichment. Several such APT experiments were carried out in different areas containing SFs and similar results were obtained, i.e. Cu depletion and In enrichment, but with different degrees of depletion or enrichment, respectively. Thus, the Cu depletion at the SFs was calculated within the interval [2.3 at.%, 4 at.%] and the In enrichment within the interval [2.3 at.%, 3.3 at.%]. Moreover, **Figure 8** (b) shows that the width of the depleted/enriched regions varies between 3 and 5 nm. This chemical width detected by APT is in concordance with the structural width detected by high-resolution TEM [9], since in the current material the SFs are more often complex involving sometimes even almost 10 atomic planes (approximately 3.6 nm with  $d_{112}=0.36$ ) [9]. However, as mentioned previously the SFs width detected by APT might be slightly biased because of possible lenses effects at the internal interfaces. Therefore, the Gibbs interfacial excess  $\Gamma$ , i.e. the number of accumulated or depleted atoms per unit interfacial area [31], is more suited to quantify the Cu depletion and In/Se enrichment at the SFs. Approximately  $10 \pm 0.4$  Cu atoms/nm<sup>2</sup> are missing and  $8.1 \pm 0.3$  In atoms/nm<sup>2</sup> and  $4.4 \pm 0.2$  Se atoms/nm<sup>2</sup> are accumulated inside the SFs. These values are averaged values over the ones obtained for the six SFs shown in **Figure 8** (a) (see Table 1). By calculating the atomic density of (112) planes ( $7.8$  at/nm<sup>2</sup>), the monolayer coverages were extracted and specified in **Table 2**. These values show that these planar faults involve more than one (112) monolayer.

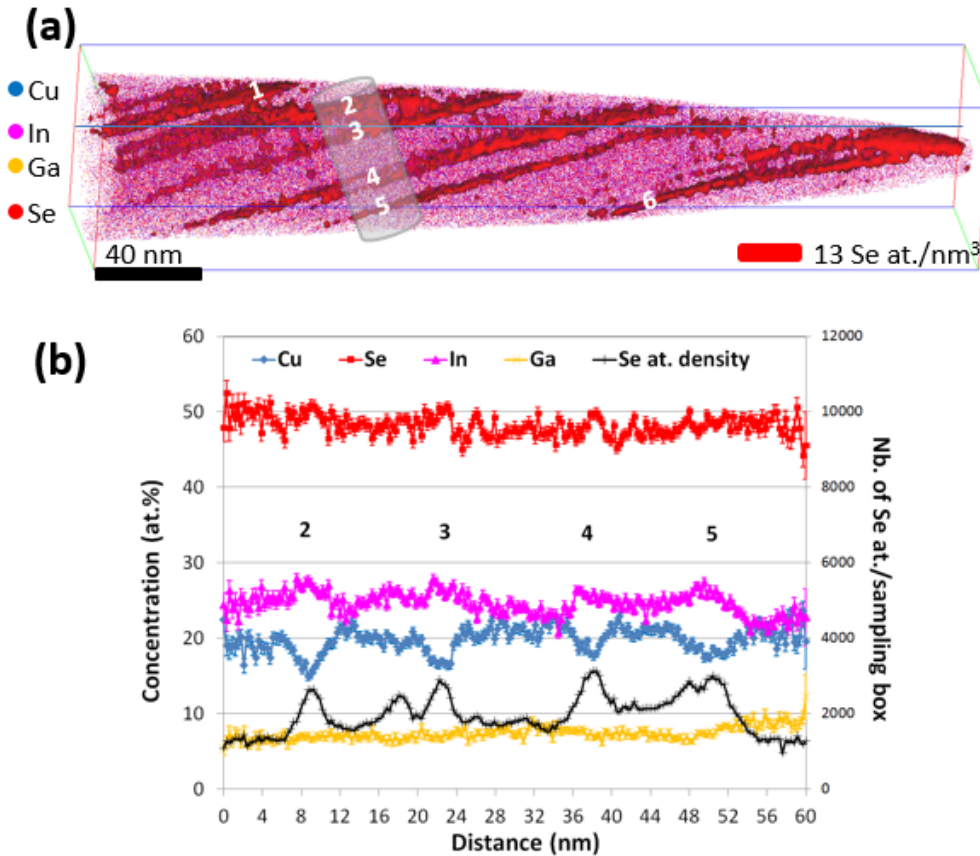


**Figure 8.** (a) 3D reconstruction of several stacking faults detected in a Cu-poor CIGS substrate. These defects are highlighted by an Se iso-density surface with a threshold value of 13 Se at./nm<sup>3</sup>. (b) Linear concentration profiles of Cu (blue), In (pink), Ga (yellow), Se (red), Na (green), K (Khaki), and O (light blue). The sampling box used to build-up these profiles is a cylinder with a diameter of 30 nm and height of 0.3 nm.

SF	$\Gamma_{\text{Cu}}$ (at/nm <sup>2</sup> )	$\Gamma_{\text{In}}$ (at/nm <sup>2</sup> )	$\Gamma_{\text{Se}}$ (at/nm <sup>2</sup> )
SF <sub>1</sub>	-8.5 ± 0.3	+8.3 ± 0.3	+8.6 ± 0.3
SF <sub>2</sub>	-10.2 ± 0.4	+7.6 ± 0.3	+6.7 ± 0.3
SF <sub>3</sub>	-8.4 ± 0.3	+5.9 ± 0.2	+6.1 ± 0.2
SF <sub>4</sub>	-10.9 ± 0.4	+8.5 ± 0.3	+5.4 ± 0.2
SF <sub>5</sub>	-14 ± 0.6	+12 ± 0.5	0
SF <sub>6</sub>	-8.6 ± 0.3	+6.6 ± 0.3	0
<b>Average</b>	-10 ± 0.4	+8.1 ± 0.3	+4.4 ± 0.2
<b>Monolayer coverage</b>	~1.3	~1	~0.6

**Table 2.** Gibbsian interfacial Excess values. The averaged values are converted into monolayer coverages, with respect to the (112) plane.

The experiments from **Figure 4** and **Figure 8** were repeated to determine the SFs composition when Na impurities are present in the CIGS absorber. **Figure 9** (a) shows the presence of one GB and three SFs inside the APT tip. Na is segregated at the GB, but not at SFs. Moreover, **Figure 9** (b) exhibits the same behavior as in **Figure 8** (b): Cu depletion and In enrichment, although the ‘In on Cu’ is not as pronounced as the one observed for the Na-free SF.

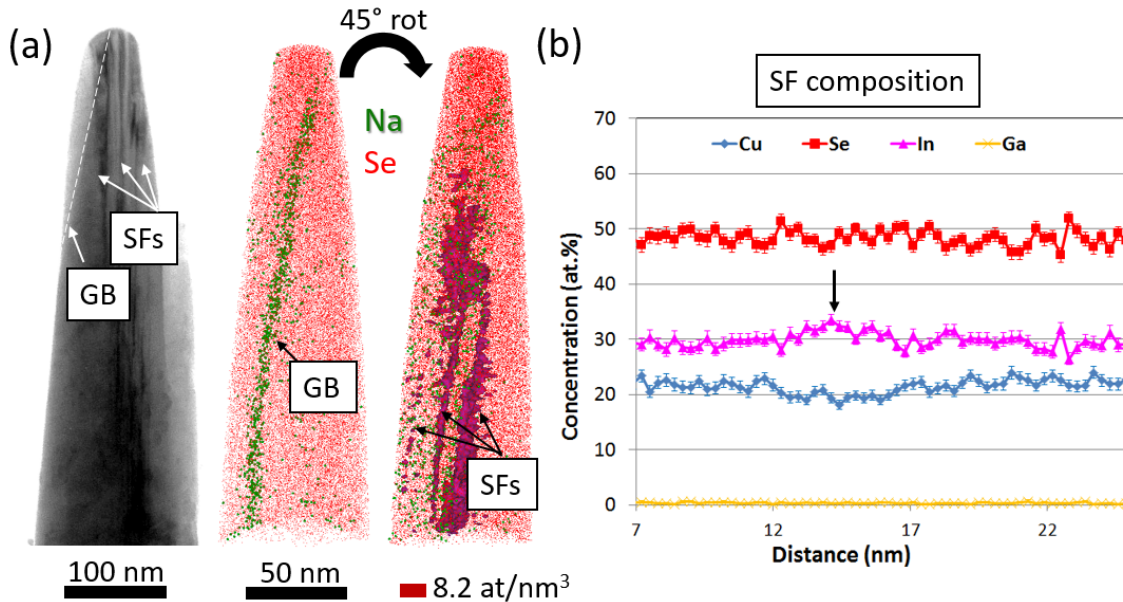


**Figure 9.** (a) TEM bright-field image of the APT tip together with the 3D APT map showing the presence of three SFs. These defects are highlighted by an Se iso-density surface with a threshold value of 8.2 Se at./nm<sup>3</sup>. (b) Linear concentration profiles of Cu (blue), In (pink), Ga (yellow), and Se (red). The sampling box used to build-up these profiles is a cylinder with a diameter of 35 nm and height of 0.3 nm.

**Figure 10** (a) shows the reconstructed 3D ion map of the coherent  $\Sigma 3$  {112} TB, which was investigated previously by STEM as shown in **Figure 5**.

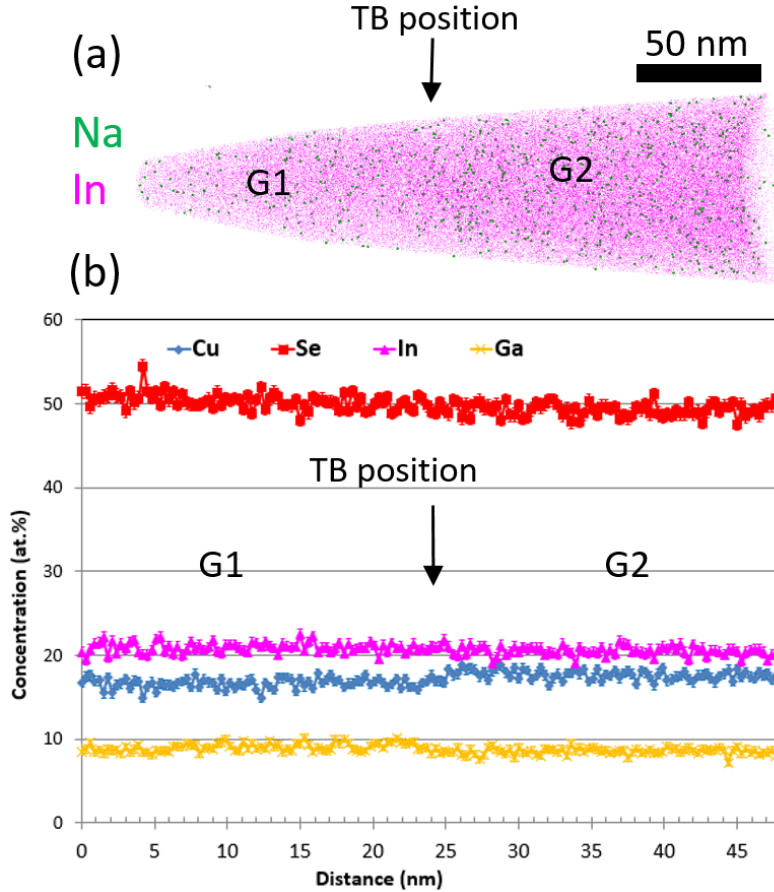


**Figure 10.** (a) 3D APT map of a  $\Sigma 3$  TB and (b) the corresponding elemental distribution profiles using a  $25 \times 25 \times 0.2 \text{ nm}^3$  sampling box.

This 3D map together with the linear concentration profiles from **Figure 10** (b) clearly reveal no impurity segregation and no change in elemental composition at the boundary plane. The slight change in Cu and Ga composition mark the transition from one grain to another in the CIGS absorber. In a previous study [12], we clearly demonstrated changes in composition from one grain to another in the CIGS absorber (G1:  $16.5 \pm 0.5$  at.% Cu,  $20.9 \pm 0.5$  at.% In,  $8.9 \pm 0.4$  at.% Ga,  $50.5 \pm 0.7$  at.% Se and G2:  $17.3 \pm 0.5$  at.% Cu,  $20.70 \pm 0.5$  at.% In,  $8.8 \pm 0.4$  at.% Ga,  $49.7 \pm 0.7$  at.% Se).

### 3.2.3 Elemental distribution at random high-angle grain boundaries

**Figure 11** shows two representative examples of random HAGBs with misorientation angles of  $28^\circ$  and  $85^\circ$ , respectively. For both GBs, we observed elemental concentration changes and Na, K, and O impurity co-segregation. Few differences are, however, observed. For the first random HAGB, **Figure 11** (a) shows indeed that Cu and Ga are depleted, whereas In is enriched ('In on Cu' scenario). This is in agreement to what was postulated by Persson et al. [32] on the basis of *ab-initio* density functional theory (DFT) calculations, namely that Cu vacancy rows are preferentially formed at the CIGS GBs. The In enrichment and the Cu depletion could be explained by the low formation energy of the charge neutral defect pair  $2V_{\text{Cu}} + \text{In}_{\text{Cu}}^{2+}$  [33]. For the second random HAGB, **Figure 11** (b) shows an opposite behavior in comparison with the previous HAGB: the Cu is not anymore depleted, but enriched. The same trend was observed for In, which in this case is depleted keeping thus the anti-correlation behavior with respect to Cu [34] ('Cu on In' scenario).

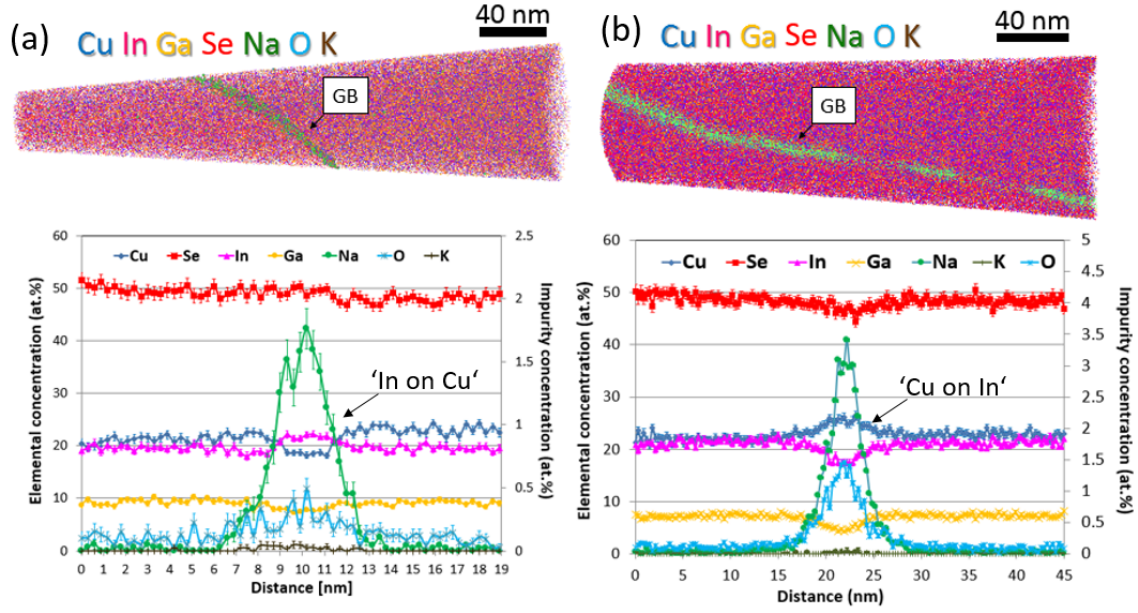


**Figure 11.** (a) and (b) 3D reconstruction showing two of the investigated GB by APT showing the distribution of Cu (blue), In (pink), Ga (yellow), Se (red), Na (green), O (light blue) and K (khaki). Linear concentration profiles of the elements and impurities. The sampling box used to construct these profiles has a volume of  $32 \times 32 \times 0.3 \text{ nm}^3$  and  $35 \times 35 \times 0.3 \text{ nm}^3$ , respectively.

Another important aspect is the Na, K, and O impurity segregation. It is believed here that these impurities diffused out of the SLG substrate into the absorber layer during the deposition of the CIGS layer at  $\sim 600 \text{ }^\circ\text{C}$ , since in this case no barrier diffusion between SLG and Mo was deposited. Moreover, random HAGBs containing no O had also been detected, which confirm that O comes from the material itself and not from APT chamber (H,  $\text{H}_2$ , and  $\text{H}_2\text{O}$  are contaminants very often found inside the APT chamber). The Na, K, and O concentrations at the first HAGB are  $1.7 \pm 0.16 \text{ at. } \%$ ,  $0.045 \pm 0.02 \text{ at. } \%$ , and  $0.5 \pm 0.08 \text{ at. } \%$ , respectively. The corresponding interfacial excesses  $\Gamma$  values for Na ( $\Gamma_{\text{Na}}$ ), K ( $\Gamma_{\text{K}}$ ), and O ( $\Gamma_{\text{O}}$ ) calculated from APT data are  $2.9 \pm 0.4 \text{ at}/\text{nm}^2$ ,  $0.075 \pm 0.05 \text{ at}/\text{nm}^2$ , and  $0.84 \pm 0.24 \text{ at}/\text{nm}^2$ , respectively. For the second HAGB, higher Na, K, and O concentration values were calculated ( $3.5 \text{ at. } \%$  Na,  $0.04 \text{ at. } \%$  K, and  $1.5 \text{ at. } \%$  O) with their respective  $\Gamma$  values of  $\Gamma_{\text{Na}} = 6.2 \pm 0.8 \text{ at}/\text{nm}^2$ ,  $\Gamma_{\text{K}} = 0.16 \pm 0.06 \text{ at}/\text{nm}^2$ , and  $\Gamma_{\text{O}} = 2.7 \pm 0.6 \text{ at}/\text{nm}^2$ .

Based on the correlative TEM-APT approach presented before, the  $\Gamma$  values as a function of misorientation angle had been determined for five  $\Sigma 3 \{112\}$  TBs and ten random HAGBs as shown in **Figure 12**.

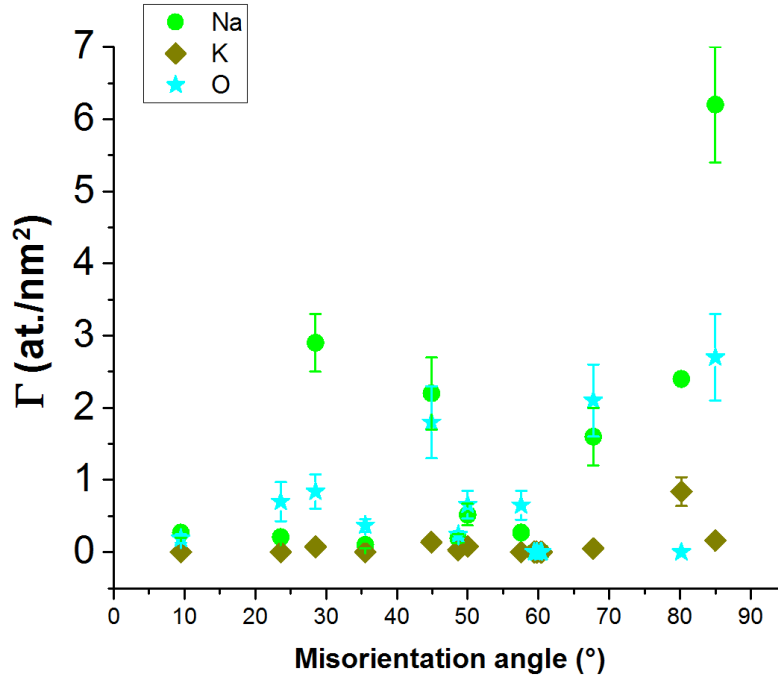


**Figure 12.** Gibbsian interfacial excess ( $\Gamma$ ) versus misorientation for one low-angle GB, five  $\Sigma 3$   $\{112\}$  TBs and ten random HAGBs.

It has been reported that the  $\Gamma_{\text{O}}$  value increases generally with the misorientation angle, whereas for  $\Gamma_{\text{Na}}$  and  $\Gamma_{\text{K}}$  no clear trend could be made. This is mainly due to the different scenarios observed for the random HAGBs as follows:

- Se-depletion at random HAGB: strong O segregation and ‘Cu on In’ behavior;
- Se-enrichment at random HAGB: no O segregation and ‘In on Cu’ behavior;
- no change in Se at random HAGB: slight O segregation and ‘In on Cu’ behavior;
- Na is always present at HAGBs. K is also believed to be found at most of the GBs, but it couldn’t be detected for some of GBs because of its very low concentration (limit detectability for K is 15 ppm).

Another important issue is the boundary curvature observed for some of the HAGBs. The curvature at the sub-micron scale correspond actually to faceted GBs at the sub-nanometer scale as it was shown recently by Stoffers et al. [35] for Si absorbers. Thus, it is expected that the boundary plane influences the impurity segregation as well. The variation of  $\Gamma_{\text{Na}}$ ,  $\Gamma_{\text{K}}$ , and  $\Gamma_{\text{O}}$  values versus the boundary plane is out of the scope of this study, since in this case correlative high-resolution STEM-APT needs to be performed.

## 4. Discussion

### 4.1 Comparison with the existing techniques

Without any knowledge of the crystallographic character of a GB, the measured chemical changes at GBs can appear contradictory. For example, Couzyine-Devy et al. [36] detected ‘In on Cu’ at GBs for a Cu-poor CIGS film ( $[\text{Cu}]/([\text{Ga}]+[\text{In}]) < 1$ ) and ‘Cu on In’ at GBs for a Cu-rich CIGS films ( $[\text{Cu}]/([\text{Ga}]+[\text{In}]) > 1$ ), whereas Raghuwanshi et al. [37] found ‘Cu on In’ GBs for a Cu-poor CIGS film, but with different Ga ratio.

Moreover, there are only few studies which correlate structure and chemistry of GBs in CIGS thin films [3, 12, 22, 34, 36, 38]. Abou-Ras et al. [3] showed by high-resolution (HR) STEM-EELS measurements the existence of Se-Se and Se-cation terminated  $\Sigma 3$   $\{112\}$  TBs. Here, the

Se-Se terminated TBs exhibit ‘In on Cu’ behavior, whereas the Se-cation terminated TBs show either Cu depletion or no change in composition. This atomic redistribution is a direct evidence for the proposed Cu-depletion at Se-Se terminated  $\Sigma 3$  {112} TBs based on first-principle calculations by Persson and Zunger [32]. Cation-cation terminated  $\Sigma 3$  {112} TBs were not experimentally found. Correlative studies for TBs with lower symmetry, i.e.  $\Sigma 9$  or  $\Sigma 27a$  TBs, which have a smaller number fraction than  $\Sigma 3$  TBs [39], have not yet been reported. Since TBs are special cases of SFs, Se-Se and Se-cation termination can also be expected for SFs. Indeed, their existence was confirmed by correlated APT-TEM studies as well as by HR-STEM-EELS, which reveal ‘In on Cu’ behavior and no atomic redistribution for these two types of SFs [40]. It was shown by HR-STEM-EELS that atomic redistribution takes place at random HAGBs as well [3, 34]. Here, an anticorrelation of Cu and In was found for CIGS GBs, i.e. ‘In on Cu’ or ‘Cu on In’, whereas the Ga does not always follow the trend of In or changes only slightly. Moreover, the APT studies exhibit that when the GB is Cu-enriched and Se-depleted then the O is strongly enriched at the boundary, and when the GB is Cu-depleted and Se-enriched then the O is not anymore detected at the boundary. The APT results presented in this work agree well with EELS-STEM observations and theory from literature [3, 33, 34]. Furthermore, our APT results show that Na segregates at random HAGBs being often accompanied by co-segregation of K and O, but no impurity segregation was observed at TBs in agreement with the work of Abou-Ras et al. [3].

Apart from planar defects, dislocations with a density of up to  $10^{10}$ - $10^{11}$   $\text{cm}^{-2}$  can be found in CIGS thin films [41]. APT revealed ‘In on Cu’ behavior as well as Na segregation at a line defect [41] in agreement with the recent high resolution STEM-EELS results on partial dislocation cores [40].

#### **4.2 Relationship between chemistry, structure, and performance for planar defects**

From the compositional analyses of various planar defects, i.e., SFs, TBs, and random HAGBs, it is apparent that the atomic planes adjacent to these planar defects appear reconstructed, as compared with the compositions in the grain interiors. All kinds of point defects, related to matrix and impurity elements, contribute to this reconstruction. Since the width of the reconstruction region (containing only the two adjacent atomic planes) is smaller than 1 nm, the issue of band offsets, which would be applied in the case of extended phases present at the planar defects, can be neglected. Therefore, when aiming at drawing conclusions on possible energy-band diagrams at the planar defects, only the present of defect states associated to the enhanced point defect density needs to be considered.

As reported by Yan et al. [42] as well as by H. Moenig et al. [43], who predicted the theoretical band diagram and analyzed the densities of state in CIGS grain interiors and at CIGS GBs, the density of deep defect states at GBs in CIGS thin films appears reduced, presumably as a consequence of the atomic reconstruction. Therefore, the defect states present at CIGS GBs (and consequently also at SFs and TBs) can be considered mostly shallow. Furthermore, these defect states are associated with bound charge densities at the planar defects, where positive charges are compensated in the *p*-type semiconductor CIGS by a depletion region (depletion of free holes) around the planar defect, while negative charges are screened by free holes. This redistribution of free charge carriers leads to upwards or downwards bending of the conduction and valence bands, which exhibits barriers for electrons or for holes.

The following considerations have been published recently in a review paper, and the reader is kindly referred to Ref. [40] for more details. The value for the upwards band bending at planar defects is limited to about +0.1 eV, by the Fermi level and therefore by the net doping concentration, which is about  $N_A=10^{16}$   $\text{cm}^{-3}$  for the best CIGS solar cell devices. The highest value for the hole barrier due to downward band bending can be estimated to about -0.1 eV from various analyses done by scanning-probe microscopy techniques [43]. Measurements by

means of electron-beam-induced current and cathodoluminescence [44] have provided low recombination velocities  $s_{GB}$  at CIGS GBs of below  $10^4$  cm/s. For negative excess charges at GBs, the screening lengths  $L_D = (\epsilon_0 \epsilon_r k_B T / e^2 N_A)^{0.5}$  (where  $\epsilon_0$  and  $\epsilon_r = 13.6$  [44] are the dielectric susceptibilities for the vacuum and for Cu(In,Ga)Se<sub>2</sub>) are in the order of about 10-100 nm. Using maximum potential-barrier heights of  $\Phi_b = 0.1$  eV, the maximum, resulting bound interfacial charge densities at grain boundaries,  $N_i = (8\Phi_b \epsilon_0 \epsilon_r N_A)^{0.5}$  [44], are about  $1 \times 10^{11}$ - $1 \times 10^{12}$  cm<sup>-2</sup>. In addition, the widths of the depletion regions (for positive excess charges at GBs),  $w = N_i / 2N_A$ , exhibit similar values of few tens of nm to few 100 nm.

The bound interfacial charge densities  $N_i$  are connected with the recombination velocities via  $s_{GB} = v_{th} \sigma N_i < 1 \times 10^4$  cm/s, with thermal velocities of  $v_{th} = 1 \times 10^7$  cm/s, which requires values for the capture cross-sections  $\sigma$  of  $1 \times 10^{-15}$ - $1 \times 10^{-14}$  cm<sup>2</sup>. Using these parameters in two-dimensional device simulations [45, 46] results in a substantial reduction of the open-circuit voltage  $V_{oc}$  of about 100 mV with respect to a device without GBs. Thus, these simulations suggest that microscopic properties of GBs, which were revealed by various experiments, may enhance nonradiative Shockley-Read-Hall recombination and thus be one reason for a reduced open-circuit voltage of CIGS solar cells.

## 5. Conclusions

In conclusion, in the present work, we showed why APT can be considered one of the standard tools for compositional analysis at the nanoscale for polycrystalline thin films. Moreover, we showed how APT can be combined with TEM to understand the link between the chemistry and structure of the extended defect. Based on various results obtained by APT and TEM, it can be stated that a common feature of planar defects in CIGS thin films is the atomic redistribution occurring in the lattice planes adjacent to the planar defects. Different redistribution schemes found at various GBs by means of APT were discussed. These APT results were compared with those from theoretical predictions, and consequences for the energy-band diagrams around these planar defects were proposed. When correlating the gathered compositional information at planar defects with results from microscopic electrical analyses at the planar defects as well as with those from two-dimensional device modeling, enhanced non-radiative (Shockley-Read-Hall) recombination, mainly at random HAGBs, is highlighted as one possible origin for the limited open-circuit voltage of the CIGS solar cells.

## Acknowledgements

The authors would like to thank the colleagues at HZB and ZSW for providing CIGS solar cells for the APT analyses, as well as Michael Herbig, Aleksander Kostka (MPI for Iron Research David Saxey (Curtin University), for their help in the TEM and APT data acquisition or interpretation. Special thanks are due to Stefan Zaefferer and Peter Konijnenberg for the TOCA software. This work was supported in part by the Federal Ministry of Education and Research (BMBF 03X5522A) and by the Helmholtz Virtual Institute VH-VI-520 ‘‘Microstructure Control for Thin-Film Solar Cells’’.

## References

1. Müller, M., et al., *Symmetry dependent optoelectronic properties of grain boundaries in polycrystalline Cu(In,Ga)Se<sub>2</sub> thin films*. Journal of Applied Physics, 2014. **115**(2): p. 023514.
2. Roselund, C. *ZSW sets new thin film solar world record with 22.6% efficient CIGS PV cell*. Industry & Suppliers 2016.

3. Abou-Ras, D., et al., *Direct insight into grain boundary reconstruction in polycrystalline Cu(In,Ga)SE<sub>2</sub> with atomic resolution*. Phys Rev Lett, 2012. **108**(7): p. 075502.
4. Adam J. Schwartz, M.K., Brent L. Adams, David P. Field, *Electron Backscatter Diffraction in Materials Science*. 2nd Edition ed. 2009: Springer.
5. Zaefferer, S., *A critical review of orientation microscopy in SEM and TEM*. Crystal Research and Technology, 2011. **46**(6): p. 607-628.
6. Randle, V., *Five-parameter' analysis of grain boundary networks by electron backscatter diffraction*. Journal of Microscopy, 2005. **222**(2): p. 69-75.
7. Herbig, M., et al., *Atomic-Scale Quantification of Grain Boundary Segregation in Nanocrystalline Material*. Physical Review Letters, 2014. **112**(12).
8. Babinsky, K., et al., *A novel approach for site-specific atom probe specimen preparation by focused ion beam and transmission electron backscatter diffraction*. Ultramicroscopy, 2014. **144**: p. 9-18.
9. Mainz, R., et al., *Annihilation of structural defects in chalcogenide absorber films for high-efficiency solar cells*. Energy Environ. Sci., 2016. **9**(5): p. 1818-1827.
10. Kaufmann, C.A., et al., *Investigation of coevaporated Cu(In,Ga)Se<sub>2</sub> thin films in highly efficient solar cell devices*. Thin Solid Films, 2007. **515**(15): p. 6217-6221.
11. Powalla, M., et al., *High-efficiency Cu(In,Ga)Se<sub>2</sub> cells and modules*. Solar Energy Materials and Solar Cells, 2013. **119**: p. 51-58.
12. Cojocaru-Miredin, O., et al., *Atomic-scale distribution of impurities in CuInSe<sub>2</sub>-based thin-film solar cells*. Ultramicroscopy, 2011. **111**(6): p. 552-6.
13. Thompson, K., et al., *In situ site-specific specimen preparation for atom probe tomography*. Ultramicroscopy, 2007. **107**(2-3): p. 131-9.
14. Herbig, M., P. Choi, and D. Raabe, *Combining structural and chemical information at the nanometer scale by correlative transmission electron microscopy and atom probe tomography*. Ultramicroscopy, 2015. **153**: p. 32-9.
15. Saxey, D.W., *Correlated ion analysis and the interpretation of atom probe mass spectra*. Ultramicroscopy, 2011. **111**(6): p. 473-9.
16. Merino, J.M., et al., *A comparative study of Cu–Se and In–Se bond length distributions in CuInSe<sub>2</sub> with related In-rich compounds*. Thin Solid Films, 2005. **480-481**: p. 295-300.
17. Schwarz, T., et al., *Atom probe tomography study of internal interfaces in Cu<sub>2</sub>ZnSnSe<sub>4</sub> thin-films*. Journal of Applied Physics, 2015. **118**(9): p. 095302.
18. Kelly, T., *Kinetic-energy discrimination for atom probe tomography*. Microscopy and Microanalysis, 2011. **17**(1): p. 1-14.
19. Miller, M.K., D. Reinhard, and D.J. Larson, *Detection and quantification of solute clusters in a nanostructured ferritic alloy*. Journal of Nuclear Materials, 2015. **462**: p. 428-432.
20. Prosa, T.J., et al. *Developing detection efficiency standards for atom probe tomography*. 2014.
21. Vurpillot, F., et al., *Modeling image distortions in 3DAP*. Microsc Microanal, 2004. **10**(3): p. 384-90.
22. Cojocaru-Mirédin, O., et al., *Characterization of Gbs in CIGS films using atom-probe tomography*. IEEE Journal of Photovoltaics, 2011. **1**(2): p. 207-212.
23. Hellman, O.C. and D.N. Seidman, *Measurement of the Gibbsian interfacial excess of solute at an interface of arbitrary geometry using three-dimensional atom probe microscopy*. Materials Science and Engineering: R: Reports, 2002. **A327**: p. 24-28.
24. Zaitsev, S., O. Shtempluck, and E. Buks, *Effects of electron beam induced carbon deposition on the mechanical properties of a micromechanical oscillator*. Sensors and Actuators A: Physical, 2012. **179**: p. 237-241.

25. Schwarz, T., et al., *Correlative t-EFSD-APT studies on CIGS grain boundaries*. Applied Physics Letters, 2016: p. in preparation.
26. Keller, R.R. and R.H. Geiss, *Transmission EBSD from 10 nm domains in a scanning electron microscope*. Journal of Microscopy, 2012. **245**(3): p. 245-251.
27. Kaigawa, R., T. Wada, and R. Klenk, *The microstructure of Cu(In,Ga)S<sub>2</sub> solar cell absorber films prepared using three-stage and two-stage evaporation*. Thin Solid Films, 2008. **516**(20): p. 7046-7050.
28. Fundenberger, J.J., et al., *Polycrystal orientation maps from TEM*. Ultramicroscopy, 2003. **96**(2): p. 127-137.
29. Zaefferer, S., *New developments of computer-aided crystallographic analysis in transmission electron microscopy*. Journal of Applied Crystallography, 2000. **33**: p. 10-25.
30. Stoffers, A., et al., *Grain boundary segregation in multicrystalline silicon: correlative characterization by EBSD, EBIC, and atom probe tomography*. Progress in Photovoltaics: Research and Applications, 2015. **23** (-): p. 1742-1753.
31. Krakauer, B.W. and D.N. Seidman, *Absolute atomic scale measurements of Gibbsian interfacial excess of solute at internal interfaces*. Physical Review B, 1993. **48**(9): p. 6724-6727.
32. Persson, C., et al., *n-type doping of CuInSe<sub>2</sub> and CuGaSe<sub>2</sub>*. Physical Review B, 2005. **72**(3).
33. Zhang, S.B., et al., *Defect physics of the CuInSe<sub>2</sub> chalcopyrite semiconductor*. Physical Review B, 1998. **57**(16): p. 9642-9656.
34. Abou-Ras, D., et al., *Confined and Chemically Flexible Grain Boundaries in Polycrystalline Compound Semiconductors*. Advanced Energy Materials, 2012. **2**(8): p. 992-998.
35. Stoffers, A., et al., *Topological segregation at faceted Si grain boundaries*. submitted to Nature Communications, 2016. **submitted**.
36. Couzinié-Devy, F., et al., *Atom probe contribution to the characterization of CIGSe grain boundaries*. IEEE, 2011. **978-1-4244-9965-6**.
37. Raghuwanshi, M., et al., *Influence of grain boundary modification on limited performance of wide bandgap Cu(In,Ga)Se<sub>2</sub> solar cells*. Applied Physics Letters, 2014. **105**(1): p. 013902.
38. Cojocaru-Miredin, O., et al., *Atom probe tomography studies on the Cu(In,g)Se<sub>2</sub> grain boundaries*. J Vis Exp, 2013. **74**: p. e50376.
39. Abou-Ras, D., et al., *Grain-boundary character distribution and correlations with electrical and optoelectronic properties of CuInSe<sub>2</sub> thin films*. Acta Materialia, 2016. **118**: p. 244-252.
40. Abou-Ras, D., et al., *Compositional and electrical properties of line and planar defects in Cu(In,Ga)Se<sub>2</sub> thin films for solar cells - a review*. physica status solidi (RRL) - Rapid Research Letters, 2016. **10**(5): p. 363-375.
41. Dietrich, J., et al., *Origins of electrostatic potential wells at dislocations in polycrystalline Cu(In,Ga)Se<sub>2</sub> thin films*. Journal of Applied Physics, 2014. **115**(10): p. 103507.
42. Yan, Y., et al., *Chemical fluctuation-induced nanodomains in Cu(In,Ga)Se<sub>2</sub> films*. Applied Physics Letters, 2005. **87**(12): p. 121904.
43. Monig, H., et al., *Direct evidence for a reduced density of deep level defects at grain boundaries of Cu(In,Ga)Se<sub>2</sub> thin films*. Phys Rev Lett, 2010. **105**(11): p. 116802.
44. Kavalakkatt, J., et al., *Electron-beam-induced current at absorber back surfaces of Cu(In,Ga)Se<sub>2</sub> thin-film solar cells*. Journal of Applied Physics, 2014. **115**(1): p. 014504.

45. Gloeckler, M., J.R. Sites, and W.K. Metzger, *Grain-boundary recombination in Cu(In,Ga)Se<sub>2</sub> solar cells*. Journal of Applied Physics, 2005. **98**(11): p. 113704.
46. Taretto, K. and U. Rau, *Numerical simulation of carrier collection and recombination at grain boundaries in Cu(In,Ga)Se<sub>2</sub> solar cells*. Journal of Applied Physics, 2008. **103**(9): p. 094523.